Geophys. J. Int. (2013) **???**, 1–12

Three-dimensional electrical conductivity in the mantle beneath the Payún Matrú Volcanic Field in the Andean back-arc of Argentina near 36.5°S: Decapitation of a mantle plume by resurgent upper mantle shear during slab steepening?

A.I. Burd[1], J.R. Booker[1], R. Mackie[2], A. Favetto[3], M.C. Pomposiello[3]

[1] *Department of Earth & Space Sciences, University of Washington, Box 351310, Seattle, Washington,* 98195*, USA*

[2] *Land General Geophysics, CGG, Via Cardinale Mezzofanti,* 34 - 20133*, Milan, Italy*

[3] *Instituto de Geocronología y Geología Isotopíca, Pabellon INGEIS, Universidad de Buenos Aires, CONICET, Ciudad Universitaria,* C1428EHA*, Buenos Aires, Argentina*

Received 2013 June 1; in original form 2013 May 15

SUMMARY

Southern Mendoza and northern Neuquén Provinces, south of the Pampean Shallow Subduction region in western Argentina, are host to the < 2 Ma Payunia Basaltic Province, which covers $\sim$39,500 km^2 with primarily basaltic intraplate volcanism. This back-arc igneous province is the result of extension due to trench roll-back following steepening of a flat slab that existed in the middle to late Miocene. Magnetotelluric data collected in 2005 and 2008 at 37 sites from 67 – 70°W and 35 – 38°S are used to probe the source of the Payún Matrú basalts. These data, which require significantly 3D structure, were used in a 3D non-linear conjugate gradient inversion. We identify two significant electrically conductive structures. One, called the SWAP (shallow western asthenospheric plume) approaches the surface beneath the Caldera Payún Matrú & the Volcán Trómen and dips westward toward the subducted Nazca slab. The second, called the DEEP (deep eastern plume) approaches the surface $\sim$100 km to the southeast and dips steeply east to 400 km depth while remaining above the subducted Nazca slab. We used a variety of model assessment techniques including both forward modeling and additional inversion to test the veracity of these features. We interpret the SWAP as the source of the < 2 Ma intraplate volcanism. Our inversion model assessment suggests that the SWAP does not need to connect to the Nazca slab. This is compatible with the lack of recent arc signature magmatism near Payún Matrú. The SWAP and DEEP are electrically connected only in the shallow crust, which is likely due to the Neuquén sedimentary basin and not a magmatic process. We propose that the SWAP and DEEP may have been more robustly connected in the past, but that the DEEP was decapitated to form the SWAP when shallow north-westward mantle flow resumed during steepening of the slab. The $\sim$2 Ma basaltic volcanism results from SWAP magma that had ponded below the crust until extension allowed eruption. The westward dipping portion of the SWAP is interpreted as mantle shear in the renewed mantle corner flow – this explains why the SWAP and Nazca slab can appear connected, yet there is no recent arc-signature magma in this region.

Key words: Payunia – Payenia – three-dimensional magnetotelluric inversion – Andino-Cuyana Basaltic Province – Mendoza Retroarc Volcanic Province – hotspot plume – Payún Matrú Volcanic Field – Complejo Efusivo Neógeno.

1 GEOLOGIC BACKGROUND

The Payunia (sometimes called Payenia) Basaltic Province (PBP) in the northern Neuquén basin of Argentina near (36.5°S, 69.5°W, see Figure 1) is a fascinating but little-studied region. This part of the Andean back-arc is south of the Pampean Shallow Subduction region near 31.5°S (Cahill & Isacks 1992; Anderson et al. 2007; Linkimer Abarca 2011) and subduction is a more normal 36°(Pesicek et al. 2012).

The present-day PBP spans $\sim$39,500 km^2 of southern Mendoza and northern Neuquén provinces and lies in the Andean back-arc approximately 150 km east of the main Andean Southern Volcanic Zone (SVZ) (Ramos & Folguera 2011). The PBP is usually divided into several sections including the Payún Matrú Volcanic Field (PMVF) which includes the area shown in browns on Fig. 1(b) and the area shown in gray to its west and south-east, the Llancanelo and Cerro Nevádo Volcanic Fields in gray to the north of the

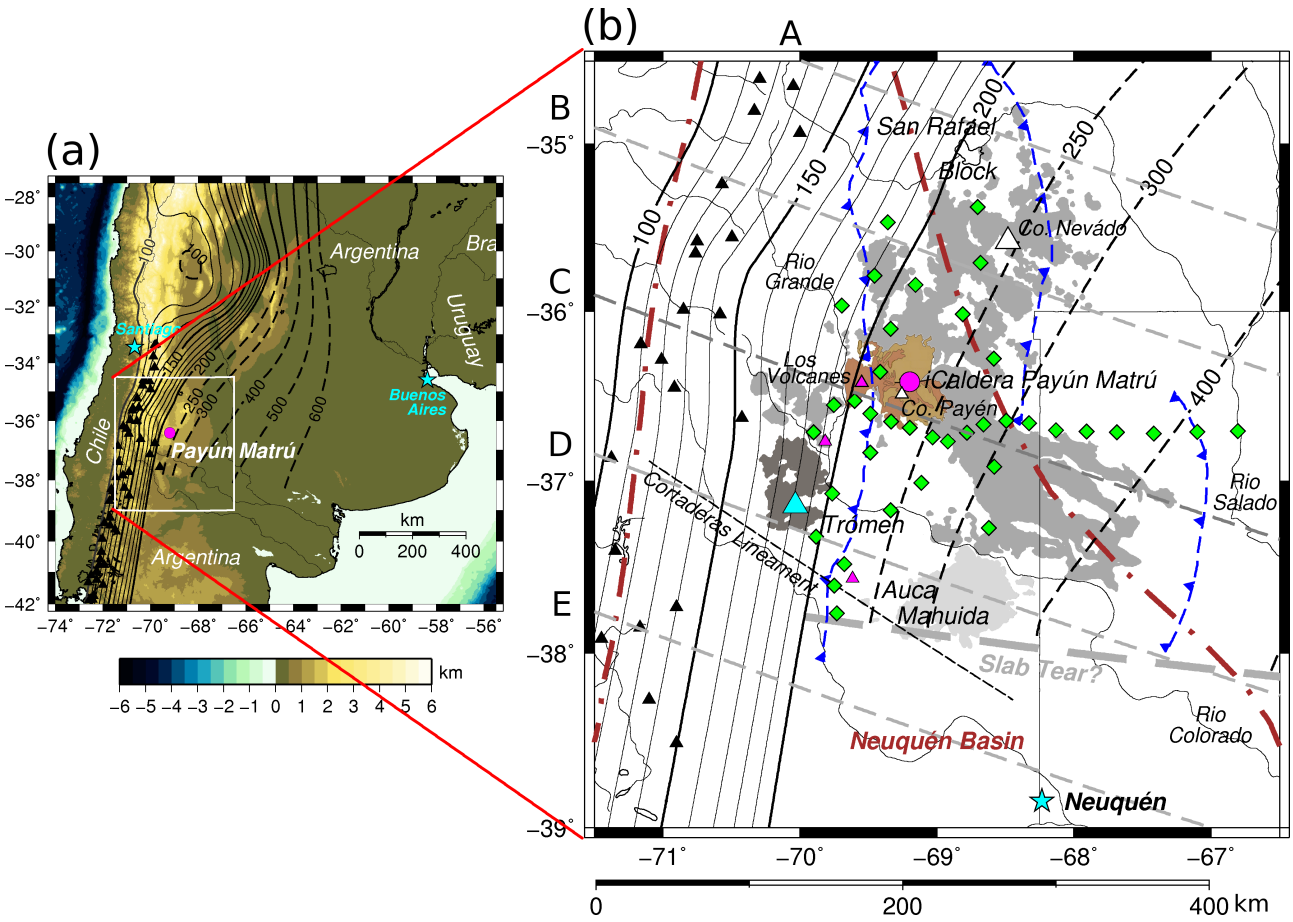

Figure 1. (a) Topography of South America, with study region in white box, active Andean Southern Volcanic Zone (SVZ) volcanoes as black triangles, Caldera Payún Matrú as a magenta circle, and contours of subducted slab (after Burd et al. (2013)) in black, with uncertain slab locations indicated with dashed black lines. (b) Payunia region, showing MT sites as green diamonds, active Andean Southern Volcanic Zone volcanoes as black triangles, Caldera Payún Matrú as a magenta circle, Volcán Trómen as a cyan triangle, Cerro Payén as a small white triangle, and Cerro Nevádo as a large white triangle. There are three small pink triangles representing geologically young activity: one is the Los Volcanes region and the other two are single monogenetic centers. Distribution of volcanics and faults is based on Ramos & Folguera (2011). The Mesozoic Neuquén Basin is outlined in brown dash-dot curves (Howell et al. 2005) and the basement thrust faults bounding the Proterozoic San Rafael Block are in blue dashed curves. The ∼1.7 Ma basaltic volcanism of the Payunia region (including the Llancanelo Volcanic Field that includes Cerro Nevádo) is in gray, with the 1.8–1.6 Ma Trómen Volcanic Field shown in darker gray and the 2–0.8 Ma Auca Mahuida Volcanic Field shown in light gray. The PMVF volcanic products younger than 200 ka are shown in tan. The Cortaderas Lineament aligns with the southern extent of the < 2 Ma volcanism, but is considered by Kay et al. (2006) to be the southern limit of a Miocene shallow subduction region. The slab tear deeper than 200 km based on tomography by Pesicek et al. (2012) is a heavy gray dashed line. Thin gray dashed lines A – E represent transects discussed in the Results section of this paper. The transects are rotated 20°clockwise to match the inversion grid, so that "North" within the grid is N20E in geographic coordinates.

PMVF, the Auca Mahuida Volcanic Field shown in light gray just south of the Rio Colorado, and the Tromen Volcanic Field shown in dark gray south-west of the PMVF.

The volcanics straddle two basement terranes: Cuyania and Chilenia. Cuyania is a sliver of Laurentia and Chilenia less certainly also from North America which were accreted to Gondwana in the Ordovician or Devonian (Ramos 2010). Payun Matru sits atop Chilenia; Cerro Nevado (see Fig. 1(b)) is on the San Rafael Block along the southwestern edge of Cuyania. Over the basement lie the Mesozoic rocks of the Neuquén Basin (outlined in Fig. 1(b)) (Howell et al. 2005). Finally, foreland units associated with the Andean Orogeny (Ramos 1999) are up to 2 km deep alongthe Rio Grande west and northwest of Payun Matru, but mostly much less.

Payunia has a complicated geologic history, but we are interested in only the last 20 Ma. Kay et al. (2006) summarize the data supporting a shallower slab and arc influenced volcanism from 20 – 5 Ma. They and Folguera et al. (2006) argue that the back-arc PBP is the result of extension due to trench roll-back and steepening of this Miocene shallow slab. Ramos & Kay (2006) conclude that the slab's steepening throughout the Pliocene and Quaternary heralded the eruption of much of the PBP's basaltic lava: during this time, the percentage of mantle melting appears to have increased and the subduction influence on the geochemistry has declined (Kay et al. 2006). However, a recent tomographic study by Pesicek et al. (2012) did not image the present-day Nazca slab deeper than 200 km south of 38°S. The compiled contours of the subducted Nazca slab (Burd et al. 2013) are shown in Fig. 1.

Volcanism in the PMVF near the Caldera Payún Matrú has been active for roughly the last 2 Ma (Ramos & Folguera 2011). Germa et al. (2010) date the Cerro Payén stratovolcano to 0.275 Ma. The Payún Matrú shield volcano collapsed to form a caldera sometime between 0.168 Ma and 0.082 Ma and is hence-

forth referred to as Caldera Payún Matrú (Germa et al. 2010). This volcano lost 25 km^3 of its total 240 km^3 during its caldera-forming eruption.

There are more than 800 volcanic vents and small cinder cones in the PBP, which have essentially no arc signature and are primarily alkalic (Bermúdez et al. 1993; Inbar & Risso 2001b). Recent work by Germa et al. (2010) indicates that the group of vents and cinder cones known as Los Volcanes to the west of the Caldera Payún Matrú range in age from ∼28 ka to younger than 7 ka and identify these lavas as basaltic to trachybasaltic. Measurements of the degradation of the shapes of these cinder cones suggests that the most recent eruption may have been about 1,000 years ago (Inbar & Risso 2001b). Based on the oral traditions of the indigenous inhabitants, Inbar & Risso (2001a) suggest that the most recent eruption could have been between 1000 and 200 years ago. Inside the Caldera Payún Matrú, Germa et al. (2010) identify trachytic lavas ranging in age from 37 ka to 7 ka. Thus, although the magma production rate is presently low, production of both basaltic and more evolved magmas almost certainly continues today. For a more comprehensive overview of Payunia, see Ramos & Folguera (2011).

The PBP volcanism is geochemically similar to intraplate basalts erupted from mantle sources undepleted of lithophile elements. These melts are often considered to arise from below the bottom of the mantle transition zone (MTZ) which spans 410 – 660 km. Bercovici & Karato (2003), however, argue that this type of volcanism need only come from the top of the MTZ. They suggest that the initial melting that strips out incompatible elements is the result of the phase change of hydrous minerals such as wadsleyite to olivine as mantle material moves upwards through the 410 km discontinuity.

Evidence that the PBP magmas have passed quickly through the crust comes from near-surface geology. Extensional features in the PBP include reactivated normal faults (Kay et al. 2006) and the relatively shallow Moho identified by Gilbert et al. (2006). Hernando et al. (2012) state that the PBP flows have $^{87}Sr/^{86}Sr$ values "suggesting little contamination with radiogenic crust." In addition, Folguera et al. (2009) also argue against a near-surface basaltic reservoir, stating that the wide distribution of monogenetic cones means that each eruption has created its own path to the surface. It is thus reasonable to conclude that the Payún Matrú source is relatively deep and interacts very little with the crust while approaching the surface.

2 METHODS

The magnetotelluric method uses passively recorded electric and magnetic field data at Earth's surface to probe electrical conductivity below Earth's surface. Electrical conductivity (with units of Siemens per meter) is strongly sensitive to changes in phase (which depends on temperature and pressure), water content, and melt fraction, but between roughly 100 and 400 km depth, elevated conductivity of upper mantle minerals are more likely the result of partial melt or other interconnected fluids than hydrous minerals (Yoshino et al. 2009). Because conductivity at dry upper mantle conditions is $<<$ 1 S/m, it is usual to use its reciprocal, resistivity (with units of Ohm-m).

Figure 1(b) shows the location of 37 MT sites collected in two field campaigns. The east-west profile was collected in 2005, while the broader array was filled out in 2008. Each site recorded 5 to 15 days of 3-component magnetic field (**H**) and horizontal components of electric field (**E**) sampled at 0.25 s with Narod Intelligent Magnetotelluric Systems (NIMS). The electric field dipoles used Pb-$PbCl_2$ electrodes (Petiau 2000).

In the frequency domain **E** and **H** are related by

$$\mathbf{E} = \begin{bmatrix} E_x \\ E_y \end{bmatrix} = \mathbf{ZH} = \begin{bmatrix} Z_{xx} & Z_{xy} \\ Z_{yx} & Z_{yy} \end{bmatrix} \begin{bmatrix} H_x \\ H_y \end{bmatrix} \quad (1)$$

where the impedance tensor **Z** is a function only of the sub-surface electric conductivity structure. The time-stationarity of **Z** allows one to estimate it using non-stationary time series of **E** and **H**. The frequency domain relation between the vertical and horizontal components of the magnetic field

$$H_z = \mathbf{W}\cdot\mathbf{H}_{horiz} = \begin{bmatrix} W_x & W_y \end{bmatrix} \begin{bmatrix} H_x \\ H_y \end{bmatrix} \quad (2)$$

defines the "induction vector" **W**. If the polarization of the source **H** is sufficently random, **W** also depends only on the sub-surface structure. **Z** and **W** have been estimated at periods from 3 to 10^4 s using the robust multi-station algorithm of Egbert (1997). All sites are processed identically so that they are directly comparable. **Z** and **W** are complex and together provide 12 data at each period and site. Only 9 periods from 20 to 5120 s are used in this study.

For the purposes of this paper, the basement rocks of the Chilenia and Cuyania Terranes are important only in that they are quite resistive ($>$ 100 Ohm-m). The skin depth (km) for penetration of electromagnetic energy is given by $\delta = 0.5\sqrt{\rho T}$ where ρ is resistivity and T is period (s). Energy with 10^3 s period penetrates 150 km through 100 Ohm-m material. The sedimentary units of the Neuquén Basin and Rio Grande foreland basin are more conductive (of order 10 Ohm-m), but the skin depth of 10 Ohm-m material at 20 s period is 7 km and substantially exceeds the maximum combined sedimentary cover. The top of the mantle is expected to have resistivity approaching 10^3 Ohm-m, decreasing to about 100 Ohm-m just above the MTZ (Yoshino et al. 2012). Basaltic melt is much more conductive (1 Ohm-m or less) and mantle containing a few percent of interconnected partial melt is at least an order of magnitude less resistive than the surrounding mantle (Schilling et al. 1997). In summary, with 20 to 5120 s data we can expect to image low resistivity materials such as partial melt in the mantle to depths of 300 km or more (Booker et al. 2004).

The magnitudes of the elements of **Z** can be significantly affected by small scale, unresolvable structure that distorts interpretation of regional structure. The most common form of this distortion is the result of electric charges that accumulate where current flows along shallow conductivity gradients. When these charges are inphase with the regional electric field, the distortion is called "static" or "Galvanic". Caldwell et al. (2004) introduced a function of the impedance

$$\mathbf{\Phi} = (Re(\mathbf{Z}))^{-1}\, Im(\mathbf{Z}) = \begin{bmatrix} \Phi_{xx} & \Phi_{xy} \\ \Phi_{yx} & \Phi_{yy} \end{bmatrix} \quad (3)$$

that is unaffacted by static distortion. $\mathbf{\Phi}$ is called the "impedance phase tensor" or simply the phase tensor. Its four elements are real and it has a preferred coordinate system in which these four data can be transformed to the direction of an ellipse axis, lengths of the ellipse semi-axes and an angle

$$\psi = \tan^{-1}\left(\frac{\Phi_{xy} - \Phi_{yx}}{\Phi_{xx} + \Phi_{yy}}\right) \quad (4)$$

called the "normalized phase tensor skew" (Booker 2013). ψ is rotationally invariant and can be computed from **Z** in any coordinate system. (Note that ψ is twice the skew angle β defined by Caldwell et al. (2004)).

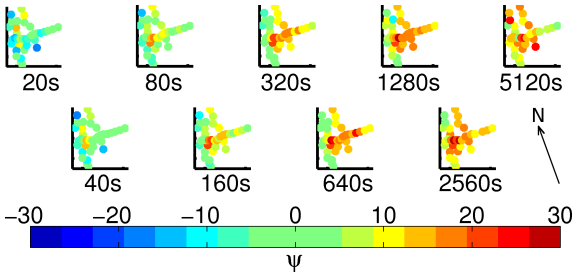

Figure 2. Plots of normalized phase tensor skew angle, ψ for observed data for all sites, at each period used in the inversion. $|\psi| < 6°$is compatible with 2D interpretation (shown in green in this figure), so most sites are clearly significantly 3D. North arrow is indicated because inversion grid (and all subsequent analyses) is rotated 20°west of N.

If the regional structure is 2D, $\psi = 0$, the phase tensor ellipse is aligned with the strike and the ellipse semi-axes are the tangents of the phases of the off-diagonal elements of the regional (i.e.undistorted) impedance. If ψ is not zero, the regional structure must be 3D. $|\psi| > 6°$is a good working criterion for concluding that the data must be 3D (Booker 2013). $|\psi| < 6°$can be considered "quasi-2D", but may still be 3D. Fig. 2 shows maps (to be referred to as "polka-dot plots") of ψ at our 37 sites. Data that meet the quasi-2D criterion of $|\psi| < 6°$are coloured green. The error bars for ψ are typically much less than 6°(see Booker (2013) for examples). It is quite clear that a preponderance of sites cannot be considered quasi-2D and thus require 3D interpretation.

Ideally, we would have incorporated the phase tensor into our inversion. However, because 3D inversion of the phase tensor is not yet sufficiently developed, we invert **Z** and **W** directly for shallow 3D structure that fits features in the data that can be the result of static distortion. However, because our site spacing is often larger than the structures causing the distortion, the details of this shallow structure are expected to be less reliable than deeper structure.

We invert the real and imaginary parts of all elements of **Z** and **W** using a 3D Non-Linear Conjugate Gradient (NLCG) algorithm ((Mackie et al. 2001; Mackie & Watts 2012; Rodi & Mackie 2012)). This seeks a model that minimizes the objective function,

$$S = \chi^2 + \tau R(m) \tag{5}$$

where τ is the trade-off parameter, $R(m)$ measures the "roughness" of the model m (also called the "structure penalty"), and

$$\chi^2 = \sum_{i=1}^{N} \frac{r_i^2}{\sigma_i^2} \tag{6}$$

is a measure of the data misfit. r_i^2 are the squares of the data residuals (i.e. predicted values – observed values), σ_i^2 are the variances, and N is the number of data.

Roughness $R(m)$ can be defined as the square of the Laplacian of the model, averaged over the model. However, because spatial resolution decreases with depth due to the diffusive physics of MT, we modify this definition so that the structure penalty in all spatial directions increases with depth. For additional discussion of $R(m)$ see Burd et al. (2013).

All models terminate in a 3 Ohm-m half-space deeper than 660 km. A deep resistivity of this order is widely accepted based on mantle conditions and minerals (Xu et al. 2000). Furthermore, Xu et al. (1998) find the phase change from olivine to wadsleyite (which occurs at roughly 410 km depth) corresponds to a two order of magnitude decrease in resistivity. Yoshino (2010) also documents a decrease in resistivity of at least an order of magnitude at 410 km. Thus there is a geophysical reason to permit a resistivity jump at 410 km. Therefore in addition to an $R(m)$ computed for the entire model, we have also performed inversions in which $R(m)$ has a tear at 410 km at which the vertical gradient of the model across this tear is excluded from computation of the roughness.

The inversions include electrically conductive oceans. They are in a coordinate system that has been rotated 20°east from geographic north to align the grid more closely to the strike of the Pacific Coast and subducted slab (see Fig. 1(a)). The importance of the Pacific Ocean in 2D inversions of our data was shown by Booker et al. (2005) and the importance of including both Pacific and Atlantic Oceans in 3D is discussed by Burd et al. (manuscript in preparation, 2013). In order to keep the mesh size relatively small while accurately modeling the effect of ocean bathymetry, we used an ocean of constant depth but varying electrical conductance. (Conductance [Siemens] = layer thickness [m] ÷ electrical resistivity [Ohm-m].) This layer has high resistivity when the water is shallow, and low resistivity when the water is deep. The ocean layers and the discontinuity between land and water are excluded from the $R(m)$ computation.

Instead of χ^2 it is common to report the "normalized RMS",

$$nRMS = \sqrt{\frac{\chi^2}{N}} \tag{7}$$

where the $nRMS$ would be 1.0 if each datum had a misfit equal to its estimated error.

Our algorithm uses weighted least squares. Data with error estimates σ_i smaller than a threshold called the "error floor" are weighted equally while data with larger error estimates are downweighted. This weighting scheme is implemented by increasing estimated uncertainties below the error floor up to the floor. Henceforth, σ_i refers to estimated data error after the error floors have been applied.

Since we are inverting the real and imaginary parts of the impedance elements, error floors are applied to these 8 data equal to 2% of the magnitudes of the off-diagonal elements $|Z_{xy}|$ and $|Z_{yx}|$. The error floors for the diagonal elements are set equal to that of the off-diagonal element in the same row. This is reasonable if the noise is primarily in the electric field. An absolute error floor of 0.01 is used for the 4 real and imaginary parts of the induction vector **W**.

These error floors are lower than commonly used for 2D inversion. 2D inversions invert apparent resistivity (related to $|\mathbf{Z}|$) and phase of off-diagonal elements. Our floors are equivalent to 4% for the apparent resistivities and 1.2° for the impedance phase. However, our inversion can still achieve $nRMS$ values close to 1.0, a rare occurence in 2D inversions even with larger error floors. This is because 3D effects in data treated as 2D can be thought of as noise. Larger misfits must be tolerated in 2D inversions to prevent a minimum structure algorithm from generating spurious structure due to fitting this "3D noise".

3 RESULTS

Figure 3 is a "trade off" diagram of $nRMS$ versus $R(m)$ for a series of 3D inversions done with decreasing values of τ in the objective function (Eq. 5). Each model is started from a smoother model with larger τ. This strategy guards against introducing unnecessarily rough structure in early iterations because NLCG algorithms

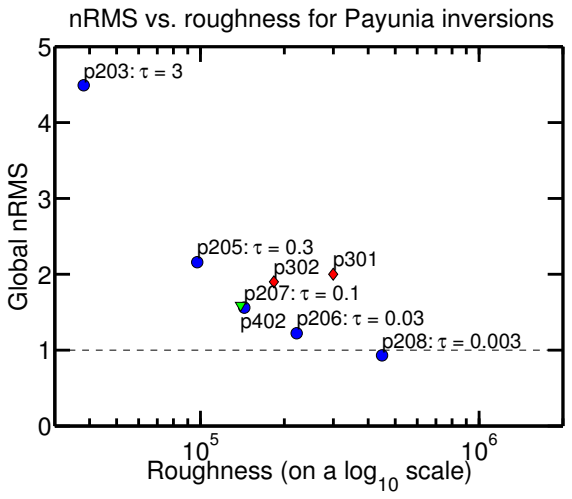

Figure 3. $nRMS$ versus roughness for Payunia inversions with different values of τ (the tradeoff parameter). Blue circles indicate the main inversion sequence, red diamonds are inversions using $\tau = 0.1$, which were used for hypothesis testing (discussed in Model Assessment section), and the green triangle is an inversion using $\tau = 0.1$ with a "tear" at 410 km depth (also discussed in Model Assessment section).

typically require a large number of iterations to remove such structure at later iterations. Also, in our experience a path through model space to an ultimately smooth model by way of much rougher models has a higher probability of being caught in local minima of the obective function.

The trade-off curve is initially steep but levels out as $nRMS$ decreases. It is below 1.0 for the roughest model p208 ($\tau = 0.003$). This model has small scale structure that we judge geologically unlikely and we have not attempted to lower the misfit futher. Models p205 to p207 share all major features. We have chosen to interpret model p207 as the best compromise between increasing the resolution while guarding against structural artefacts due to fitting noise. Polka dot plots of the $nRMS$ by site and period are shown for p207 in Figure 4. We see that the misfits are fairly "white" (distributed uniformly with space and period) except at the shortest period. It is not surprising that the misfit is larger at the shortest period because we do not have enough site density to accurately model the very shallow structure.

"Fence" plots with nominally east-west slices of model p207 are shown together with two resistivity isosurfaces in Figure 5(a – c) (note that Fig. 1(b) shows slices A – E, which are rotated 20°clockwise from east-west to match the inversion grid, so that "North" within the grid is N20E in geographic coordinates). We focus on two major features: (1) a conductive structure visible in slices B, C, and D that dips steeply eastward just above the Nazca slab to near the top of the transition zone at 400 km, which we call the DEEP (DEep Eastern Plume); and (2) a conductor visible in slices C and D that dips westward to meet the subducted slab at about 150 km. We call this structure the SWAP (Shallow Western Asthenospheric Plume). The DEEP and SWAP are separated by a resistive zone roughly 100 km wide at most depths.

The details of the SWAP are best seen in the smaller scale resistivity isosurface (Fig. 5(c)). It appears to have a foot on the slab and then rises to a conductive body with significant north-south extent near the top of the mantle. This north-south structure has two obvious protrusions from its top. One rises directly up into the shallow crust under Caldera Payún Matrú (shown as a magenta

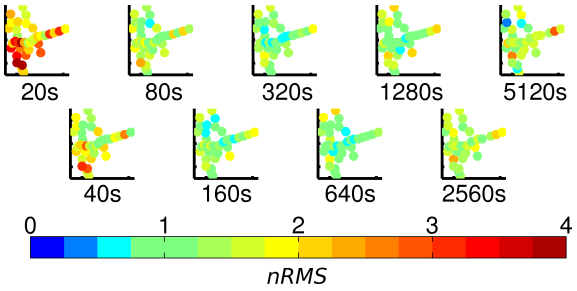

Figure 4. Maps showing $nRMS$ at each site at each period for p207. Site locations are indicated by the coloured circles, where the colour corresponds to the $nRMS$ at that site. Note that $0.75 < nRMS < 1.25$ are green to indicate sites at which the inversion was able to adequately fit the data. Note that the fit is spatially white: fit is equally good at all sites with no particular region being especially poorly fit. Fit is also approximately white by period with the exception of the larger $nRMS$ values at the shortest period. See text for discussion of why the misfit is not as good at the shorter periods.

circle in Fig. 5(b – c)). The second rises up close to the geologically young Volcán Trómen (shown as a black triangle in Fig. 5(b – c)).

3.1 Model Assessment

Fig. 5(d) shows the results of inversion p402, which has a "tear" at 410 km depth. p402 is fully converged and shown as a green triangle on Fig. 3: the global $nRMS$ value is comparable to p207, but $R(m)$ can not be directly compared to the other inversions shown in the figure because $R(m)$ for p402 does not include values at the tear's location. If the data were not sensitive to structure below the depth of the tear, the region below the tear would have resistivity values identical to the bottom boundary condition of 3 Ohm-m because that is the smoothest possible structure below the tear. Structure below 410 km is visible in all slices, so the data are sensitive to structure below the depth of the tear. In addition, structure above the depth of the tear appears very similar to structure in p207. We conclude that upwards smoothing of the fixed bottom boundary has little effect on the model above 410 km.

Seismologists commonly investigate resolution of their 3D inversions using "checkerboard" tests. Data are generated for a model consisting of an array of blocks alternating about the large scale average structure. These are inverted to see how well the blocks can be recovered. This is not as useful in our case because MT data respond most strongly to model features which constrain current to flow along extended continuous paths. An important by-product of this fact is that MT data can sense stucture outside of an array.

In a sense, our inversions are already a resolution test because we find models that have the least complexity for given levels of data misfit. Thus the smallest spatial scales seen in the model tell you the resolution. An important caveat, however, is that this is only meaningful if you are not fitting data noise.

However, questions that need addressing include whether a given model feature is an artefact of the structure penalty used to define minimum structure and whether alternate models exist that have different structure but have the same value of the objective function (Eq. 5). Such models are often called "equifeasible".

A model artefact that is constrained solely by the structure penalty will not alter the predicted data (within the measurement uncertainties) if the structure is removed. This is tested by removing structures and recomputing the predicted data. We can, however, go a step further and restart the inversion from the altered model

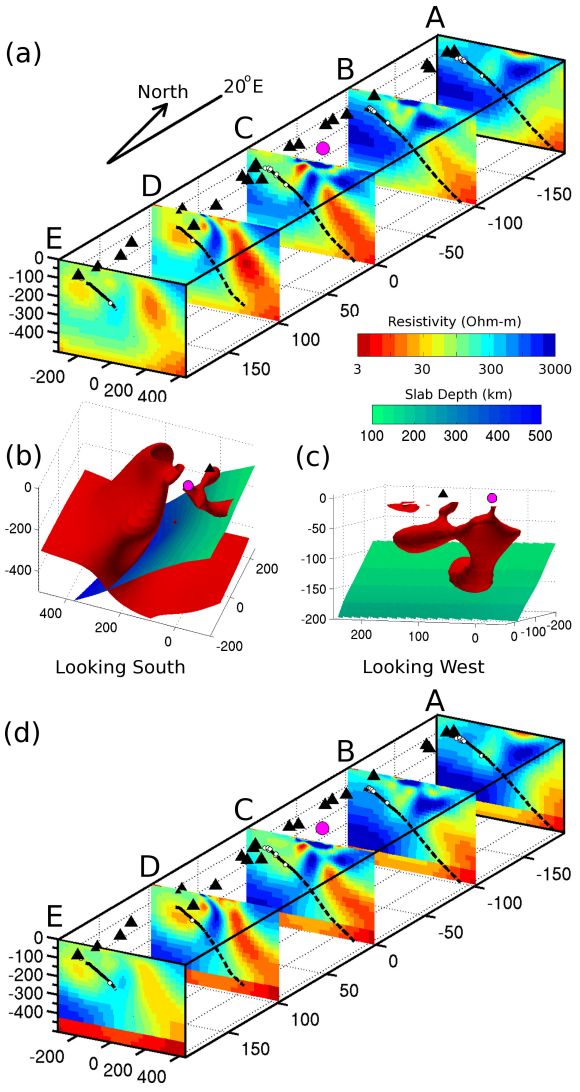

Figure 5. (a) Nominally East-West slices of resistivity for inversion p207. Slice positions are shown on Fig. 1(b). Black triangles are Southern Volcanic Zone volcanoes active in the Holocene, magenta circle is location of Caldera Payún Matrú, black lines and dashed black lines are location of subducted Nazca slab, based on the slab surface discussed in Burd et al. (2013). White points are earthquakes. Scale is stretched North-South to improve viewing. The origin (0,0) = 69.5°W, 36.5°S. X-axis and Y-axis are measured in km from this origin, and Z-axis is depth in km. (b) 35 Ohm-m isosurface of resistivity, showing DEEP to left and SWAP to right (in red), with subducted slab in green – blue. Volcán Trómen is the black triangle and Caldera Payún Matrú is the magenta circle. Isosurface is looking directly south and shows model deeper than 32 km (i.e. is mantle only). (c) shows only SWAP's 35 Ohm-m isosurface, but has same legend as (b), except image looks directly west and model is not shown shallower than 8 km. (d) Nominally East-West slices of resistivity for inversion p402, which has a "tear" at 410 km depth (discussed in text). Same caption as Fig. 5(a).

constraining the region of removed structure to remain fixed. If the inversion cannot find a model with an objective function value as low as the original model, we have confidence that the structure is required. Our confidence will be even higher if this new inversion converges to a model that re-establishes current paths clearly similar to the original model given that it cannot use the region where the removed structure existed. If this new inversion finds a model with an equal objective function, we have found an equifeasible model. If the the objective function is actually smaller for the new model, we can conclude that the original inversion was caught in a "local minimum" of the objective function.

We have identified two major structures that will be tested: the DEEP and the SWAP. For each we have performed three tests:

(1) Remove the entire structure and re-converge the inversion while preventing the original structure from reforming.
(2) Remove depth segments to find out which have significant influence on the data.
(3) Block vertical current flow at specific depths to find out whether the structure must be electrically continuous.

Because the mantle background is approximately 100 Ohm-m, structure is removed by a thresholding scheme in which values below 100 Ohm-m are replaced by 100 Ohm-m. This allows the structure to cease to exist without creating new contrasting structure and reduces the model roughness.

Vertical current flow is blocked with thin horizontal 10000 Ohm-m tablets at the desired depths. These extend beyond the plume region that can be clearly identified as being less resistive than the background but not so far as to intefere with regional vertical currents associated with features like the oceans.

We are inverting 3996 data (12 responses at 9 periods at 37 sites). Judging the misfit changes for such a large number of data requires defining measures that are diagnostic and can be compactly presented. We use two characteristic ratios. The first is the ratio of $nRMS$ of the test model to its unperturbed value $nRMS_0$. For brevity, we write

$$P = \frac{nRMS}{nRMS_0} \tag{8}$$

The second is the absolute change in normalized phase tensor skew angle relative to its estimated error, which we write:

$$\delta\psi_\sigma = \frac{|\psi - \psi_0|}{\sigma} = \frac{|\Delta\psi|}{\sigma} \tag{9}$$

where σ is the estimated error of ψ with error floors applied. These are viewed as a function of period and site using the polka dot plots introduced in Fig. 2. Their more global values can be presented in tables (such as Table 1).

P is sensitive to data misfit in a way that would not depend on data error if all uncertainties were equal. $\delta\psi_\sigma$ is sensitive to changes in model dimensionality that affect the responses (as opposed to affecting only the roughness). When $P = 1$ there has been no change in $nRMS$, when $P < 1$ the $nRMS$ has decreased (unlikely, but still a possibility), and when $P > 1$ the $nRMS$ has increased. More importantly, when $P > 2$, it means that the misfit of every datum has on average doubled, which represents very significant worsening of the fit. When $\delta\psi_\sigma < 1$ then $\Delta\psi$ is insignificant relative to its error, when $1 < \delta\psi_\sigma < 2$ then $\Delta\psi$ is moderately in excess of its error, and when $\delta\psi_\sigma > 2$ then $\Delta\psi$ is at least twice the size of its error. P is useful because it includes both impedance tensor and vertical field data. If all data had the same errors, the error would cancel out of P and P would not depend on the error. In practice, however, data do not all have the same errors, but in our inversions, the error floors make the data errors similar in size and thus P depends only weakly on estimated error and choice of error floor. $\delta\psi_\sigma$ is useful because it is unaffected by shallow distortion, combines all elements of the impedance tensor and is sensitive to changes in structural dimensionality.

In polka dot plots, values of both ratios less than one are green because these values mean that the structural change is allowed by

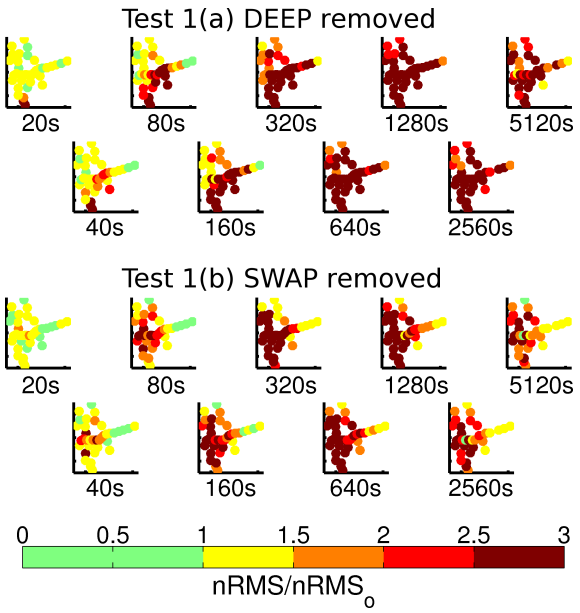

Figure 6. Map views showing $P = nRMS/nRMS_0$ at each site at each period with the DEEP removed (Test 1(a) as discussed in the text) and SWAP removed (Test 1(b)). Green values are considered insignificant change from the original model. Note that the effect of removing either plume is larger at longer periods.

the data and thus we cannot assign geological importance to the structure being tested. We use the following P-test criteria to identify tests for which a change in structure has strongly affected the data: if $P > 1$ at many sites or $P > 2$ at a few sites, then we can be confident that the original structure is not an artefact. Since $\delta\psi_\sigma$ is primarily related to the change in dimensionality of the model and the tests only change the structure near the DEEP or SWAP, we expect $\delta\psi_\sigma$ to be much more localized than P. Thus the following $\delta\psi_\sigma$-test criteria identify tests for which the change in dimensionality of the structure is considered significant: $\delta\psi_\sigma > 1$ at many sites or $\delta\psi_\sigma > 2$ at a few sites.

3.1.1 Tests 1 (a & b): Existence of the Plumes

Figure 6 shows polka dot plots of P at all periods when the DEEP and SWAP are removed from model p207. P is greater than 2 across most of the spectrum with the changes peaking over each plume and at longer periods for the DEEP. 1280 s is strongly affected for both structures and to simplify discussion we present only this period for other tests. Table 1 further charcterizes the distribution of misfit at 1280 s. Based on Table 1, there is only one site with $P < 2$ for removal of the DEEP and only 10 sites with $P < 2$ for the SWAP.

Figure 7 shows $\delta\psi_\sigma$ at 1280 s. The region of $\delta\psi_\sigma > 2$ is more spatially concentrated than P, but is still large at a significant number of sites.

Figure 8 plots convergence of the objective function S after re-starting inversions from p207 with each plume removed and the original plume location "frozen" so that the plume is forbidden to return to its original location. The final $nRMS$ and roughness $R(m)$ for each case are plotted as points p301 and p302 on the trade-off diagram (Fig 3). P and $\delta\psi_\sigma$ test results at 1280 s are shown in Table 1: all four test criteria for significant change are met for each test. Removal of the DEEP moves the trade-off point

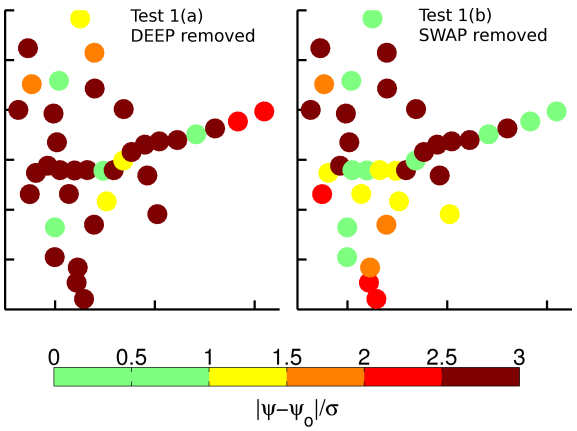

Figure 7. Map views showing $\delta\psi_\sigma$ at each site at 1280 s with the DEEP removed (Test 1(a) as discussed in the text) and SWAP removed (Test 1(b)). Green values are considered insignificant change from the original model.

further from p207 than removal of the SWAP, but in both cases $nRMS$ and $R(m)$ are substantially larger than for model p207. Thus the objective function is considerably larger. We conclude that both plumes are not artefacts and are required by our field data.

Slices and mapviews of models p301 and p302 (with p207 for comparison) are shown in Figure 9 and are quite interesting. We have dubbed the features around the former DEEP and SWAP "halo-plumes" because in each case the inversion has constructed conductive paths around the excluded volume. Thus there is little doubt that the DEEP and SWAP exist. A remarkable coupling exists between the two halo-plumes. Removing the DEEP makes the SWAP more conductive and removing the SWAP makes the DEEP more conductive. We interpret this to mean that the model requires a specific amount of vertical current flow to fit the data: if the current can't flow through one plume, it tries to increase current flow through the other plume to compensate.

3.1.2 Tests 2 (a – g) – Introduction of Gaps in the Plumes

The point of these tests is to systematically test the depth extent of the two plumes by examining the sensitivity of the data to the removal of segments of each plume. For the DEEP we remove segments: (a) from 100 to 347 km; (b) from 5 to 100 km; (c) from 5 to

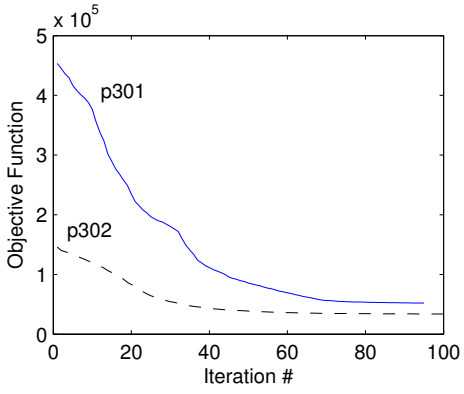

Figure 8. A plot of objective function versus number of iterations for p301 and p302 shows that each inversion's objective function has converged.

Table 1. Hypothesis test results at 1280 s. A total of 37 sites were used at this period for both the P-tests and the $\delta\psi_\sigma$-tests: columns other than Global $nRMS$ indicate the number of sites in each category. See text for discussion of each test. Global $nRMS$ represents $nRMS$ at all sites and periods used in the inversion. For comparison, global $nRMS$ for p207 is 1.560.

Test No.	Global $nRMS$	$1 < P < 2$	$P > 2$	$1 < \delta\psi_\sigma < 2$	$\delta\psi_\sigma > 2$	Test Description
1a	4.812	1	36	5	28	removal of DEEP from 4.6 km – 347 km
1b	3.486	10	27	9	18	removal of SWAP from 6.8 km – 199 km
2a	2.455	12	25	4	28	removal of DEEP from 103 km – 347 km
2b	4.319	8	29	7	25	removal of DEEP from 4.6 km – 103 km
2c	3.290	15	19	12	11	removal of DEEP from 4.6 km – 32.6 km
2d	2.006	22	10	8	8	removal of DEEP from 12.9 km – 32.6 km
2e	2.382	21	10	8	4	removal of DEEP from 4.6 km – 12.9 km
2f	3.214	12	25	10	15	removal of SWAP from 32.6 km – 199 km
2g	1.991	30	5	6	5	removal of SWAP from 6.8 km – 32.6 km
3a	1.579	22	0	2	0	vertical current block of DEEP at 347 km
3b	1.966	27	8	6	25	vertical current block of DEEP at 199 km
3c	2.545	16	21	6	27	vertical current block of DEEP at 103 km
3d	2.670	15	20	7	18	vertical current block of DEEP at 32.6 km
3e	2.431	16	17	9	10	vertical current block of DEEP at 12.9 km
3f	2.490	23	14	8	10	vertical current block of SWAP at 32.6 km
301	2.001	31	4	5	14	converged inv., model "frozen" at Test 1a DEEP location
302	1.900	31	5	8	15	converged inv., model "frozen" at Test 1b SWAP location

32 km; (d) from 13 to 32 km; (e) from 5 to 13 km. For the SWAP we remove: (f) below 32 km and (g) from 7 to 32 km. The 1280 s period results are presented in Table 1. All four of the P and $\delta\sigma_\psi$ criteria for significant change are met for each test. Together these tests support the full depth extent of each feature.

3.1.3 Tests 3 (a – f): Vertical Current Blocking

When structure is 1D, MT source fields induce only horizontal current flow. Conductive plumes channel horizontally induced current into the vertical direction. To investigate how deep the current source must be, we can block the flow at successively deeper depths. Additionally we can investigate how far the plumes extend into the crust by blocking vertical current flow within the crust. Vertical current blocks were placed in the DEEP at (a) 347 km; (b) 199 km; (c) 100 km; (d) 32 km; and (e) 13 km. The only current block in the SWAP was placed at (f) 32 km. The results of these tests at 1280 s are summarized in Table 1. All four of the P and $\delta\sigma_\psi$ criteria for significant change are met for Tests 3b – 3f, but not for Test 3a. Test 3a may be flawed because the surrounding mantle is conductive enough at this depth that the vertical current flow was not fully blocked by the resistive tablet. Together these tests support vertical current flow through the full depth extent of the DEEP and vertical current flow through the crust-mantle boundary of the SWAP.

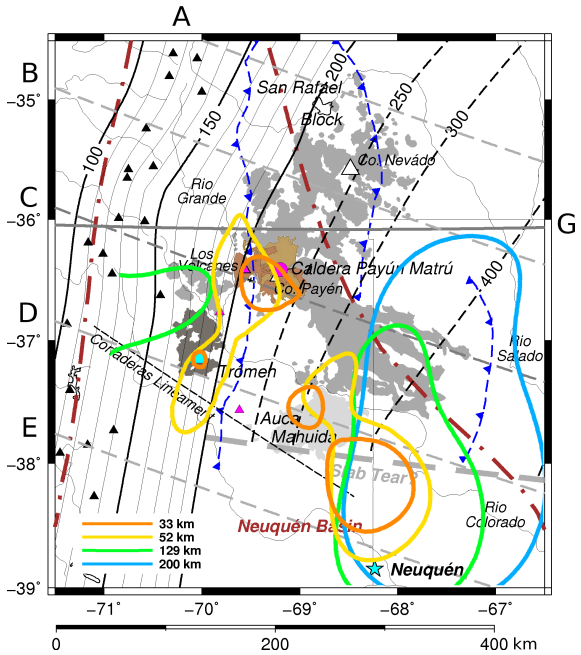

Figure 10. Figure is identical to Fig. 1(a), with addition of contours corresponding to 35 Ohm-m isosurface of DEEP and SWAP at 33, 52, 129, and 200 km. Transect G shows position of seismic receiver function work of Gilbert et al. (2006) discussed in connection with Fig. 11.

4 DISCUSSION

4.1 Comparison of SWAP & DEEP to regional geology

Figures 5(b – c) and 10 show that the SWAP has two conductive tendrils that approach the surface. One tendril is directly under the Caldera Payún Matrú. The other tendril is 100 km southwest of the Caldera Payún Matrú, directly under the Trómen Volcanic Field (TVF), which comprises the south-west portion of the PBP.

The TVF is similar to the rest of the PBP in age and composition. In particular, the TVF's most recent volcanism has no arc signature and is interpreted to be from an intraplate source (Ramos & Folguera 2011). As no information about local volcanism was used in our inversions, the positioning of the SWAP tendrils is unlikely to be fortuitous.

The SWAP is east of both the expected mantle wedge location

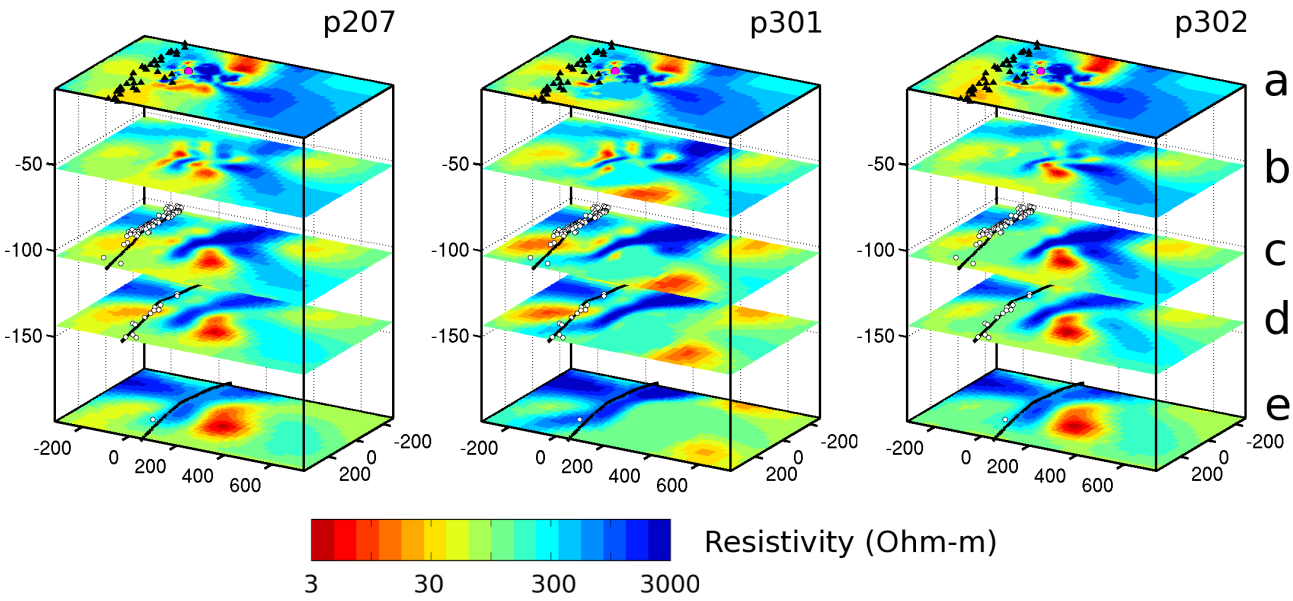

Figure 9. Map legend same as Fig. 5(a), but images are map-view slices of resistivity through models p207, p301, and p302 at different depths. Map-views' "east-west" direction is parallel to slices A – E shown on Fig. 1(b), with each horizontal slice taking up roughly the area spanned by the five original east-west slices.

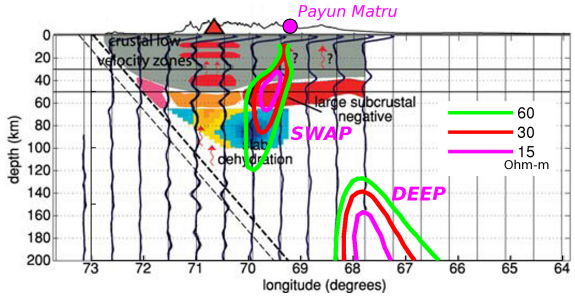

Figure 11. 60, 30, and 15 Ohm-m contours for SWAP and DEEP from slice C of Figs. 1(b) and 5(a), superimposed on a receiver function-derived diagram from Gilbert et al. (2006) that corresponds to transect G on Fig. 10.

(visible in slice C of Figure 5(a)) and the main Andean volcanic arc. The SWAP remains above the subducted Nazca slab, with the most conductive part of the SWAP at ∼50 km depth. Figs. 5(a) and 10 show that the SWAP dips west, apparently intersecting the subducted Nazca slab's location at ∼130 km depth. If the SWAP were connected to the slab, the recent volcanic products at the PBP could be expected to show an arc signature. However, since recent volcanism shows no arc signature, it is plausible that the SWAP does not connect to the subducted Nazca slab. In fact, while deeper portions of the DEEP were re-created in inversion p301 (section 3.1.1) and shown in Fig. 9 (p301), the deeper portion of the SWAP seems to have disappeared from inversion p302 (Fig. 9 (p302)). The SWAP is thus not required to extend to the subducted Nazca slab's location at 130 km depth.

Fig. 11 shows that the SWAP coincides with the large subcrustal negative arrival identified by Gilbert et al. (2006) and Wagner et al. (2005) using receiver function analysis. Gilbert et al. (2006) suggest that this subcrustal negative is related to the back-arc volcanism. The SWAP's superposition with this negative arrival lends credence to our assertion that the SWAP is related to the root of the PBP volcanism.

Unlike the SWAP, Figures 5(a) and 10 show that the DEEP dips to the east, entering the top of the Mantle Transition Zone (MTZ) at roughly 400 km while remaining above the subducted Nazca slab. The DEEP can not be positively identified below 400 km, so it is not clear whether the DEEP rises from near the top of the MTZ or from a deeper source.

While the DEEP does not appear to "connect" to the Earth's surface directly under the Caldera Payún Matrú, it does approach the surface beneath the portion of the PBP known as the Auca Mahuida Volcanic Field (AMVF) 100 km southeast of the Caldera Payún Matrú (Fig. 10). The AMVF is geochemically and geochronologically similar to the rest of PBP, but with no volcanism younger than 0.8 Ma (Ramos & Folguera 2011).

While the Payunia area shows obvious evidence of extension, a topographic profile along slice C (see Fig. 10) in Fig. 12 shows evidence of uplift and a significant change in topographic slope at the marked scarp. The footprint of the shallow portion of the DEEP correlates with this region of uplift and suggests that the DEEP has directly influenced this uplift.

While a fairly strong resistor (>1000 Ohm-m) separates the DEEP and SWAP by at least 100 km at most depths (see Fig. 5(a)), it is possible that the DEEP and SWAP are connected shallowly above ∼7 km. In fact, slice a of Fig. 9 (p207), taken at ∼5 km, shows conductivity beneath the PBP that spans the location of DEEP and SWAP. Shallower than ∼5 km (DEEP) and ∼7 km (SWAP), the model was generally more conductive, and it was not possible to positively identify either DEEP or SWAP for additional model assessment. This electrically conductive shallow connection almost certainly stems from increased water within the Neuquén basin sedimentary rock that underlies much of the PBP. There is a single young mono-genetic volcanic center between the TVF and Auca Mahuida Volcanic Field (see Fig. 10), but no other evidence of < 2 Ma volcanism between the TVF and the Auca Mahuida Volcanic Field. Given additional evidence against a PBP near-surface basaltic reservoir (Hernando et al. 2012; Folguera et al. 2009), the shallow electrical connection between DEEP and SWAP is unlikely to represent partial melt.

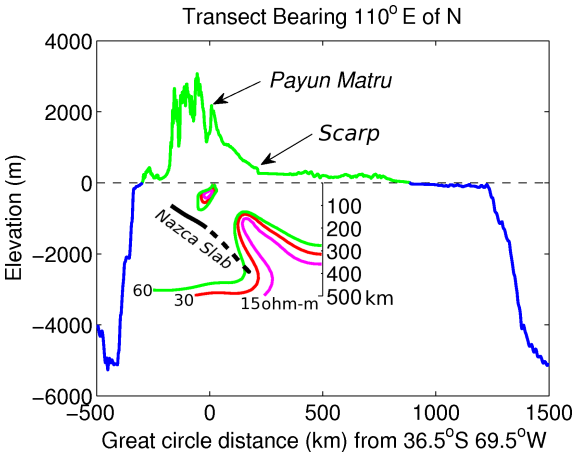

Figure 12. Topographic transect along slice C of Figs. 5(a) and 10 shows depth of both Pacific and Atlantic Oceans. Inset shows SWAP, DEEP, and subducted Nazca slab, also from slice C: shallowest portion of DEEP corresponds to marked scarp, while SWAP corresponds to Payún Matrú.

4.2 Comparison to other electrical conductivity models

A structure closely resembling the DEEP was previously identified by Burd et al. (2008) as a result of a 2D MT inversion using a subset of the 37 sites included in this paper's work. This result (shown in Ramos & Folguera (2011)) was interpreted to indicate current flow between MTZ and the shallow crust. It appeared to surface under the PMVF, which suggested a deep source for the PMVF volcanism. However, Figure 10 shows that the DEEP surfaces over 100 km to the south-east, at the Auca Mahuida Volcanic Field. This earlier 2D work was likely negatively affected by the attempt to fit 3D data with a 2D model.

The DEEP has strong similarities to, but significant differences from, a deep conductive plume studied by Burd et al. (2013). This deep "flatslab" plume is 600 km north of the DEEP and just east of the region of Pampean Shallow Subduction. The flatslab plume is capped at 100 km depth where Burd et al. (2013) suggest it cannot penetrate compressive lithosphere, while the DEEP appears to rise into the crust.

An additional important difference is that the flatslab plume penetrates the down-dip extrapolation of the flatslab while the DEEP remains parallel to the projected subducted Nazca slab as depth increases. Burd et al. (2013) invoke a slab window to explain the flatslab plume's interaction with the slab. However, while there is no need for a slab window above 400 km at the DEEP location, the slab and the DEEP would intersect in the MTZ. There are two possible scenarios. First, the slab does not extend below 400 km (and there is no evidence that it does) and does not exist south of the tear suggested by Pesicek et al. (2012) (shown in Fig. 10). In this case, the DEEP could continue through the MTZ into the DEEP mantle. In the second scenario, the slab below 400 km is responsible for generating the DEEP, perhaps by local introduction of water into the MTZ.

Newberry Volcano in Oregon, USA, in the back-arc of the Cascades appears to be arguably similar to the PMVF and PBP. Egbert et al. (2012) identify an arguably 500 km deep electrically conductive plume similar to our DEEP rising vertically beneath Newberry. Newberry and the Cascadia Subduction Zone have been studied extensively, with Long et al. (2012) proposing that the Miocene shallow slab steepening and trench roll-back drive westward mantle corner flow, subsequent upper plate extension and back-arc volcanic upwelling.

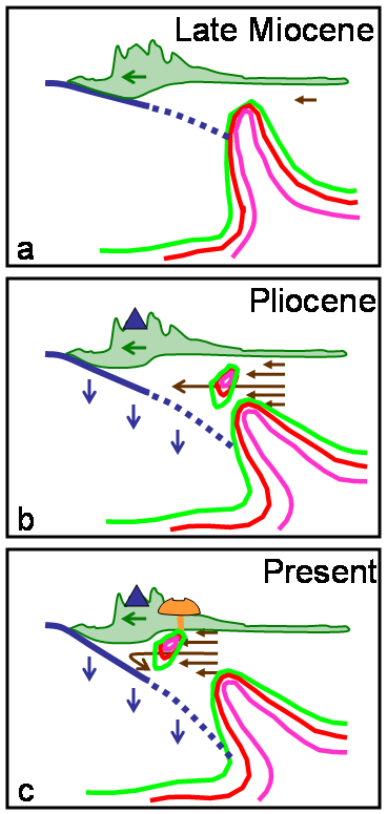

Figure 13. Three cartoons depicting evolution of present-day PBP, SWAP, and DEEP. 60, 30, & 15 Ohm-m contours of SWAP & DEEP in green, red, & magenta; subducted Nazca slab location in solid or dashed blue line; Nazca slab motion vectors in blue; mantle flow vectors in brown; PBP in tan; active SVZ at dark blue triangle. (a) shows situation during the end of the Miocene shallow subduction regime, when DEEP and SWAP were one structure just beginning to be sheared north-westward; (b) slab steepening continues through Pliocene, causing increase in mantle flow which shears SWAP and DEEP to north-west, eventually decapitating DEEP to form SWAP; (c) present-day situation based on slice C of Fig. 5 – SWAP, DEEP, Nazca slab are to scale, with South America, SVZ, and PBP at correct locations but with exaggerated height.

4.3 DEEP & SWAP: indicators of mantle flow

Our SWAP and DEEP are compatible with an interpretation related to Long et al. (2012)'s Cascadia discussion applied to the Andean back-arc. As the subducted slab steepens, the mantle must flow into the region between the slab and the lithosphere. The largely intraplate signature of the < 2 Ma PBP volcanism is compatible with this mantle flow (Germa et al. 2010; Kay et al. 2006). Gilbert et al. (2006) also propose that mantle corner flow may play a role in the back-arc volcanism of this region. If there is also a slab tear south of 38°S as suggested by Pesicek et al. (2012), this flow would be towards the north-west rather than due west, as material wells up around the southern edge of the Nazca slab.

We propose that this northwesterly flow has decapitated the DEEP to form the SWAP. During the Miocene shallow subduction regime, the SWAP was a part of the DEEP (Fig. 13(a)). However, as trench roll-back and slab deepening began to occur at the begin-

ning of the Pliocene, the SWAP was sheared off and pulled to the north-west (away from the DEEP) as mantle flowed into the area formerly occupied by the Nazca slab (Fig. 13(b)). The contours and slab location in Fig. 13(c) are not a cartoon – they are from slice C of Fig. 5(a) as shown on Fig 12. In this interpretation, the depth of greatest horizontal displacement of the SWAP from the DEEP represents the depth of greatest upper mantle flow velocity. Thus the SWAP tilts downward to the north-west and the DEEP tilts upward to the north-west, indicating greatest flow velocity near 130 km depth. Given additional time, as trench rollback & slab deepening continue and the DEEP continues to rise to the surface, the DEEP will continue to be caught in the mantle shear to the north-west and may undergo additional decapitation. If this process continues, we might expect renewed volcanism at Auca Mahuida.

The mantle flow velocity under South America since the Pliocene has the same order of magnitude as South America's velocity relative to the deep mantle. South America is moving 45 km/Ma in a hot-spot reference frame, so over 5 Ma (since the beginning of the Pliocene) the SWAP has likely moved $\sim$225 km. SWAP and DEEP are separated by $\sim$200 km at 130 km depth, which is compatible with our estimation of SWAP movement.

In our mantle-flow interpretation, the PBP should have been more active in the past when extension associated with the trench roll-back and slab deepening first allowed eruption of the pond of SWAP magma that had formed at the base of the compressional crust during the Miocene shallow subduction regime. Some volcanism associated with the SWAP continues to occur, but the magma flux is much less than it was 1.7 Ma ago (Germa et al. 2010; Ramos & Folguera 2011).

5 CONCLUSION

3D minimum-structure inversions of magnetotelluric data yield an image of the electrical conductivity beneath the Payún Matrú Volcanic Field in western Argentina. We have demonstrated the existence of an electrically conductive plume (the DEEP) that extends from 5 km below Payunia (and possibly shallower) to at least 347 km depth, dipping to the east and remaining above the subducted Nazca slab. We have also demonstrated the existence of an electrically conductive plume (the SWAP) that extends from 7 km (and possibly shallower) below the Caldera Payún Matrú and the Trómen Volcanic Field to roughly 130 km depth, dipping to the west and remaining above the subducted Nazca slab. While the DEEP has relatively constant conductivity at all depths, the SWAP is most conductive near 50 km depth.

The DEEP and SWAP conductivity and the PBP volcanism are best explained by a partially melted mantle plume. This plume has been sheared by the north-westward shallow mantle corner flow to form the previously connected SWAP and DEEP.

6 DATA AVAILABILITY

The MT data used in this paper are available through the IRIS Data Management System, Seattle, Washington.

ACKNOWLEDGMENTS

This project is supported by the U.S. National Science Foundation (NSF) Grants EAR9909390, EAR0310113 and EAR0739116 and U.S. Department of Energy Office of Basic Energy Sciences grant DE-FG03-99ER14976. MT equipment is from the EMSOC Facility supported by NSF Grants EAR9616421 and EAR0236538. This project also received support from the Agencia Nacional de Promoción Científica y Tecnológica PICT 2005 No. 38253. The first author received support from the Seattle Chapter of the ARCS Foundation, and from Graduate Reseach Support, Qamar, Stephens, and Coombs Fellowships provided by the Dept. of Earth and Space Sciences, University of Washington. Thank you to Jimmy Larsen for numerous helpful discussions. Gabriel Giordanengo of Instituto de Geocronología y Geología Isotopíca provided extensive assistance in the field.

REFERENCES

Anderson, M., Alvarado, P., Zandt, G., & Beck, S., 2007. Geometry and brittle deformation of the subducting Nazca Plate, Central Chile and Argentina, *Geophysical Journal International*, **171**, 419–434.

Bercovici, D. & Karato, S., 2003. Whole mantle convection and the transition-zone water filter, *Nature*, **425**, 39–44.

Bermúdez, A., Delpino, D., Frey, F., & Saal, A., 1993. Los basaltos de retroarco extrandinos, *Geologia*, pp. 161–172, Ramos, V. ed. Geologia y recursos naturals de Mendoza, Relatorio, XII Congreso Gelologico Argentino y II Congreso Exploration de Hydrocarburos, Assoc. Geol Argentina y Inst, Argentino del Petroleo, may not be an article.

Booker, J. R., 2013. The Magnetotelluric Phase Tensor: A Critical Review, *Surveys in Geophysics*.

Booker, J. R., Favetto, A., & Pomposiello, M. C., 2004. Low Electrical Resistivity associated with plunging of the Nazca flat slab beneath Argentina, *Nature*, **429**, 399–403.

Booker, J. R., Favetto, A., Pomposiello, M. C., & Xuan, F., 2005. The roll of fluids in the Nazca flat slab near 31s revealed by the electrical resistivity structure, in *6th International Symposium on Andean Geodynamics, Barcelona, Spain, Extended Abstracts*, pp. 119–122, IRD Editions, 2005, ISBN: 2-7099-1575-8.

Burd, A. I., Booker, J. R., Pomposiello, M. C., Favetto, A., Larsent, J., Giordanengo, G., & Orozco Bernal, L., 2008. Electrical conductivity beneath the Payún matrú volcanic field in the andean back-arc of argentina near 36.5°S: insights into the magma source, in *7th. International Symposium on Andean Geodynamics, Nice, France, Extended Abstracts*, pp. 90–93, CHECK ME.

Burd, A. I., Booker, J. R., Mackie, R. L., Pomposiello, M. C., & Favetto, A., 2013. Electrical conductivity of the Pampean Shallow Subduction Region of Argentina near 33°S: evidence for a slab window, *Geochemistry Geophysics Geosystems*, In revision, MS No. 2013GC004732.

Cahill, T. & Isacks, B., 1992. Seismicity and Shape of the Subducted Nazca Plate, *Journal of Geophysical Research*, **97**, 17503–17529.

Caldwell, G. C., Bibby, H. M., & Brown, C., 2004. The Magnetotelluric Phase Tensor, *Geophysical Journal International*, **158**, 457–469.

Egbert, G., 1997. Robust multiple-station magnetotelluric data processing, *Geophysical Journal International*, **130**, 475–496.

Egbert, G. D., Meqbel, N., Wannamaker, P., Schultz, A., & Kelbert, A., 2012. Three-dimensional Inversion of EarthScope Magnetotelluric Data: crustal and mantle conductivity beneath the NW USA, IRIS Webinar.

Folguera, A., Zapata, T., & Ramos, V., 2006. Late Cenozoic extension and the evolution of the Neuquen Andes, in *Evolution of the Andean Margin: A tectonic and magmatic view from the Andes to the Neuquen Basin (35-39S lat)*, vol. 407, pp. 267–286, eds Kay, S. & Ramos, V., Geological Society of America.

Folguera, A., Naranjo, J. A., Orihashi, Y., Sumino, H., Nagao, K., Polanco, E., & Ramos, V. A., 2009. Retroarc volcanism in the northern san rafael block (34°– 35°30′s), southern Central Andes: Occurrence, age, and tectonic setting, *Journal of Volcanology and Geothermal Research*, **186**, 169–185.

Germa, A., Quidelleur, X., Gillot, P. Y., & Tchilinguirian, P., 2010. Volcanic evolution of the back-arc Pleistocene Payun Matru volcanic field, Argentina, *Journal of South American Earth Sciences*, **29**, 717–730.

Gilbert, H., Beck, S., & Zandt, G., 2006. Lithospheric and upper mantle structure of central chile and argentina, *Geophysical Journal International*, **165**, 383–398.

Hernando, I. R., Llambías, E. J., González, P. D., & Sato, K., 2012. Volcanic stratigraphy and evidence of magma mixing in the quaternary Payún Matrú volcano, andean backarc in western argentina, *Andean Geology*, **39**, 158–179.

Howell, J. A., Schwarz, E., Spalletti, L. A., & Veiga, G. D., 2005. The Neuquén Basin: an overview, in *The Neuquén Basin, Argentina: A Case Study in Sequence Stratigraphy and Basin Dynamics*, vol. 252, pp. 1–14, Geological Society, London.

Inbar, M. & Risso, C., 2001a. Holocene Yardangs in Volcanic Terrains in the Southern Andes, Argentina, *Earth Surface Processes and Landforms*, **26**, 657–666.

Inbar, M. & Risso, C., 2001b. A morphological and morphometric analysis of a high density cinder cone volcanic field – Payun Matru, south-central Andes, Argentina, *Zeitschrift fur Geomorphologie*, **45**(3), 321–343.

IRIS Data Management System, Seattle, Washington, 2013. The facilities of the IRIS Data Management System, and specifically the IRIS Data Management Center, were used for access to waveform, metadata or products required in this study. The IRIS DMS is funded through the National Science Foundation and specifically the GEO Directorate through the Instrumentation and Facilities Program of the National Science Foundation under Cooperative Agreement EAR-0552316. Some activities of are supported by the National Science Foundation EarthScope Program under Cooperative Agreement EAR-0733069.

Kay, S. M., Burns, W., Copeland, P., & Mancilla, O., 2006. Upper Cretaceous to Holocene magmatism and evidence for transient Miocene shallowing of the Andean subduction zone under the northern Neuquen Basin, in *Evolution of the Andean Margin: A tectonic and magmatic view from the Andes to the Neuquen Basin (35 – 39S lat)*, vol. 407, pp. 19–60, eds Kay, S. M. & Ramos, V. A., Geological Society of America.

Linkimer Abarca, L., 2011. *Lithospheric Structure of the Pampean Flat Slab (Latitude 30-33S) and Northern Costa Rica (Latitude 9-11N) Subduction Zones*, Ph.D. thesis, University of Arizona, Tucson, Arizona.

Long, M. D., Till, C. B., Druken, K. A., Carlson, R. W., Wagner, L. S., Fouch, M. J., James, D. E., Grove, T. L., Schmerr, N., & Kincaid, C., 2012. Mantle dynamics beneath the Pacific Northwest and the generation of voluminous back-arc volcanism, *Geochemistry Geophysics Geosystems*, **13**(1).

Mackie, R. L. & Watts, M., 2012. Detectability of 3-D sulphide targets with AFMAG, *SEG Technical Program Expanded Abstracts*, pp. 1–4.

Mackie, R. L., Rodi, W., & Watts, M. D., 2001. 3-D magnetotelluric inversion for resource exploration, in *SEG 2001 Technical Program Expanded, San Antonio, Texas*.

Pesicek, J. D., Engdahl, E. R., Thurber, C. H., DeShon, H. R., & Lange, D., 2012. Mantle subducting slab structure in the region of the 2010 M8.8 Maule earthquake (30–40°S), Chile, *Geophysical Journal International*, **191**, 317–324.

Petiau, G., 2000. Second Generation of Lead-lead Chloride Electrodes for Geophysical Applications, *Pure and Applied Geophysics*, **157**(3), 357–382.

Ramos, V. A., 1999. Los depósitos sinorogénicos terciarios de la región andina, in *Geología Argentina*, vol. 29, pp. 651–682, ed. Caminos, R., Servicio Geológico Minero Argentino (SEGEMAR).

Ramos, V. A., 2010. The Grenville-age basement of the andes, *Journal of South American Earth Sciences*, **29**, 77–91.

Ramos, V. A. & Folguera, A., 2011. Payenia volcanic province in the Southern Andes: An appraisal of an exceptional Quaternary tectonic setting, *Journal of Volcanology and Geothermal Research*, **201**, 53–64.

Ramos, V. A. & Kay, S. M., 2006. Overview of the tectonic evolution of the southern Central Andes of Mendoza and Neuquen (35 39s latitude), in *Evolution of the Andean Margin: A tectonic and magmatic view from the Andes to the Neuquen Basin (35- 39S lat)*, vol. 407, pp. 1–17, eds Kay, S. & Ramos, V., Geological Society of America.

Rodi, W. L. & Mackie, R. L., 2012. The inverse problem, in *The Magnetotelluric Method Theory and Practice*, pp. 347–420, eds Chave, A. D. & Jones, A. G., Cambridge University Press.

Schilling, F. R., Partzsch, G., Brasse, H., & Schwarz, G., 1997. Partial melting below the magmatic arc in the central Andes deduced from geoelectromagnetic field experiments and laboratory data, *Physics of the Earth and Planetary Interiors*, **103**, 17–31.

Wagner, L. S., Beck, S. L., & ME, G. Z. F., 2005. Upper mantle structure in the south central chilean subduction zone (30 to 36s), *Journal of Geophysical Research*, **FIX ME**, FIX ME.

Xu, Y., Brent, T., Poe, T., Shankland, T., & Rubie, D., 1998. Electrical conductivity of olivine, wadsleyite and ringwoodite under upper-mantle conditions, *Science*, **280**, 1415–1418.

Xu, Y., Shankland, T., & Poe, T., 2000. Laboratory-based electrical conductivity in the earth's mantle, *Journal of Geophysical Research - Solid Earth*, **105**(B12), 27865–27875.

Yoshino, T., 2010. Laboratory Electrical Conductivity Measurement of Mantle Minerals, *Surveys in Geophysics*, **31**, 163–206.

Yoshino, T., Matsuzaki, T., Shatskiy, A., & Katsura, T., 2009. The effect of water on the electrical conductivity of olivine aggregates and its implications for the electrical structure of the upper mantle, *Earth and Planetary Science Letters*, **2008**, 291–300.

Yoshino, T., Shimojuku, A., Shan, S., Guo, X., Yamazaki, D., Ito, E., Higo, Y., & Funakoshi, K., 2012. Effect of temperature, pressure and iron content on the electrical conductivity of olivine and its high-pressure polymorphs, *Journal of Geophysical Research*, **117**.